`MagLens`: Bringing Mobile, Fine-Grained Imaging to Ferrous Building Structures

Jike Wang
Shanghai Jiao Tong University
Shanghai, China
jikewang@sjtu.edu.cn

Yasha Iravantchi
Stanford University
Stanford, USA
yasha@stanford.edu

Mingke Wang
The University of Michigan, Ann Arbor
Ann Arbor, USA
mingkew@umich.edu

Alanson Sample
University of Michigan
Ann Arbor, USA
apsample@umich.edu

Kang G. Shin
The University of Michigan
Ann Arbor, USA
kgshin@umich.edu

Xinbing Wang
Shanghai Jiao Tong University
Shanghai, China
xwang8@sjtu.edu.cn

Dongyao Chen*
Shanghai Jiao Tong University
Shanghai, China
chendy@sjtu.edu.cn

Abstract

Fine-grained inspection of ferrous structures, such as steel rebars and iron pipes, is essential for ensuring structural health/integrity. However, existing non-destructive imaging techniques often suffer from coarse spatial resolution, high operational costs, and limited mobility support, hence severely restricting their practical deployment. For example, ground-penetrating radar (GPR), constrained by its operating wavelength, cannot resolve sub-centimeter features or recover fine contours of embedded ferrous structures.

We present `MagLens`, a mobile and cost-effective imaging system for inspecting ferrous structures, such as rebars, metal studs, and iron pipes. Leveraging high-sensitivity commercial-off-the-shelf (COTS) magnetometers, `MagLens` introduces two key designs: (1) a novel synthetic aperture of magnetic sensors (SAMS) that combines a compact hardware, a rotation-based scanning module to enhance spatial coverage and an optional pre-magnetization module for extending the sensing range; and (2) a physics-informed neural imaging pipeline trained on synthetic data, enabling robust contour reconstruction and depth estimation with minimal effort. By capturing precise cross-sectional contour variations, `MagLens` can achieve corrosion assessment. We evaluate `MagLens` in diverse real-world settings using rebars as a representative structural material, achieving high-fidelity imaging that captures fine-grained geometries, e.g., bending, intersecting, and parallel layouts. `MagLens`' efficacy is also tested on iron pipes, metal studs, and irregular objects, e.g., garden shears, not seen during the training phase. Results show that `MagLens` achieves contour reconstruction errors within 1 mm and depth estimation errors below 0.5 cm.

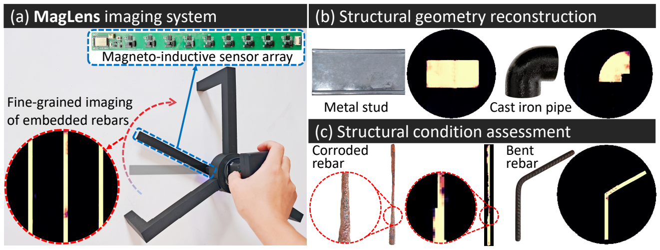

Figure 1: (a) illustrates the mobile form factor of `MagLens` for imaging embedded ferrous structures; (b) and (c) show reconstruction of diverse geometries and condition assessment.

CCS Concepts

- **Hardware → Sensor devices and platforms**.

Keywords

Magnetic Sensing; Magnetic Imaging; Structure Inspection

ACM Reference Format:
Jike Wang, Yasha Iravantchi, Mingke Wang, Alanson Sample, Kang G. Shin, Xinbing Wang, and Dongyao Chen. 2026. `MagLens`: Bringing Mobile, Fine-Grained Imaging to Ferrous Building Structures. In *ACM/IEEE International Conference on Embedded Artificial Intelligence and Sensing Systems (SenSys '26), May 11–14, 2026, Saint Malo, France.* ACM, New York, NY, USA, 15 pages. https://doi.org/10.1145/3774906.3802749

1 Introduction

Ferrous materials such as iron and steel are foundational to modern infrastructure [29, 83]. In buildings, steel rebars provide tensile reinforcement for concrete, galvanized metal studs support wall framing, and iron pipelines transport water, gas, and industrial chemicals. The long-term integrity of these concealed components is critical, as their degradation can compromise structural integrity and leads to catastrophic failures. For example, the collapse of a Surfside, Florida condominium, which resulted in 98 deaths, was attributed to prolonged corrosion of rebars [14]. Corrosion or cracking in pipelines

---

[*] Dongyao Chen is the corresponding author.

SenSys '26, Saint Malo, France

ACM ISBN 979-8-4007-2309-4/26/05
https://doi.org/10.1145/3774906.3802749

can damage surrounding structural elements and compromise overall building safety [33, 47]. To mitigate such risks, recent US and EU regulations mandate recurring structural inspections [11, 12, 26], making fine-grained inspection essential for determining precise spatial attributes (e.g., depth, geometry) and assessing the condition (e.g., corrosion levels) of ferrous structures, enabling early detection of degradation and preventing catastrophic failures.

However, fine-grained inspection of ferrous structures remains challenging. Destructive methods, such as drilling and electrochemical corrosion tests [80], require *invasive access*, *substantial labor*, and *structural compromise*. For example, for drilling concrete, the noise level of rotary hammer and core drills can easily exceed 110 dB [24]. This destructive process also incurs extensive time and labor costs. Non-destructive techniques also suffer key limitations. Ultrasonic approaches suffer from severe signal attenuation and scattering in heterogeneous media such as concrete [52, 69]. Ground-penetrating radar (GPR) offers coarse spatial resolution due to long wavelengths [5]. Millimeter-wave imaging [50, 51, 91] exhibits poor penetration in concrete [82, 95], with signal attenuation exceeding 10 dB/cm [62]. While IR-UWB radar systems [49, 95] improve penetration, they produce coarse confidence maps, lacking the spatial resolution to recover geometric details such as rebar diameter. Infrared thermography is highly sensitive to surface texture and environmental temperature variations [65, 86]. Electromagnetic detectors (e.g., rebar locators) are low-cost and portable but can only indicate target *presence*, without reconstructing fine-grained geometry or assessing material degradation such as corrosion.

Compared to conventional sensing modalities, magnetic fields can penetrate non-magnetic materials such as concrete and are robust to environmental interference such as water and mud [87, 88]. Ferrous structures exhibit remanent magnetization induced during manufacturing, which persists over time (Sec. 2.2.2). By capturing these magnetic fields, sensors such as Hall-effect magnetometers enable visualization of magnetic fields and inference of object geometry [39, 67, 84]. However, existing magnetic sensing systems suffer from short sensing range, prohibitive hardware complexity, and limited geometric reconstruction capability. For example, most systems rely on *static* 2D sensor arrays that require extremely close proximity to the target ($<$ 5 mm [67]), thus impractical for mobile scanning applications. They also demand dense, high-resolution magnetometer arrays, with hardware costs exceeding \$50,000 [25], limiting their practicality and affordability. Commercial solutions [21, 28] employ proprietary hardware to detect magnetic field anomalies for diagnosing structural degradation (e.g., rebar corrosion) but still rely on external tools for precise detection (i.e., position/depth) and lack fine-grained geometric reconstruction.

We present `MagLens`, a novel mobile imaging system that enables high-resolution reconstruction of embedded ferrous structures using low-cost, off-the-shelf magnetometers. To address the limited sensing range and coarse imaging resolution of existing magnetic sensing systems, `MagLens` incorporates two key designs: (1) **Synthetic aperture of magnetic sensors (SAMS)**, which combines a compact and cost-efficient hardware design, a rotation-based scanning mechanism and an optional pre-magnetization module. This design supports mobile deployment and achieves high spatial coverage with a minimal number of sensors. (2) **Physics-informed neural imaging pipeline**, which reconstructs both the geometric contour and cover depth of ferrous structures from raw magnetic field measurements. This joint reconstruction recovers critical structural attributes of ferrous objects, including fine-grained shapes, spatial position, and material degradation such as corrosion.

Synthetic aperture of magnetic sensors. To enable high-resolution imaging of ferrous structures in a compact form factor, `MagLens` addresses two main challenges. First, conventional 2D arrays are costly and impractical for mobile deployment. Second, magnetic signals from ferrous structures are inherently weak. For example, metal studs produce field strengths below 10 μT at a 5 cm distance (Sec. 4.1). To overcome these limitations, `MagLens` adopts a motion-enabled virtual aperture design that integrates high-sensitivity magnetometers. As shown in Fig. 1(a), `MagLens` employs nine COTS inductive magnetometers (PNI RM3100 [7]) arranged in a compact linear layout (21.4 cm × 1.8 cm) at a cost $<$ \$150. Compared to Hall-effect sensors, RM3100 offers 23× higher resolution [7], enabling reliable detection of weak magnetic fields. To achieve fine-grained spatial resolution, we introduce a rotational scanning scheme tailored for magnetic sensing, inspired by the synthetic aperture concept [73]. Specifically, the sensor array is mounted on a motorized platform to collect multi-angle magnetic data around the target. `MagLens` also contains an optional *pre-magnetization* module that magnetizes the target before scanning, amplifying weak residual fields and thus extending the sensing range further. Combined with our robust imaging pipeline, `MagLens` accurately inspects ferrous structures at 11 cm cover depth (Sec. 7.3.1), which is sufficient for real-world walls [9, 10].

Physics-informed neural imaging pipeline. Accurately imaging ferrous structures from raw magnetic readings presents three key challenges. First, collecting large-scale real-world data is impractical due to high operational cost and limited accessibility of embedded structures. Second, magnetic patterns vary with object geometry, depth, and orientation, requiring a model that generalizes across diverse scenarios. Third, the measured field reflects the combined effects of geometry (e.g., bending, cross-section loss) and magnetization state (e.g., different ferrous materials, remanence magnitude/direction), introducing ambiguity that hinders the reconstruction performance. To address these issues, `MagLens` presents a neural imaging pipeline that reconstructs key object attributes, including geometry and spatial position. For scalable training, we propose a physics-inspired, voxelized magnet modeling framework that approximates a ferrous object as an array of aligned passive magnets, enabling efficient synthesis across diverse geometries and spatial configurations *consistent* with structural codes [10, 16]. To mitigate geometry–magnetization ambiguity, we randomize remanence magnitude and direction during synthesis on fixed geometry (Sec. 5.2). We then apply normalization to suppress amplitude/offset variations and preserve geometry-relevant patterns. The imaging network adopts a transformer-enhanced Swin-UNet [40] that jointly predicts a contour mask and a scalar cover depth. Requiring only 2.6% of real data for fine-tuning, `MagLens` delivers high-fidelity contour reconstruction with depth estimation error below 0.5 cm (Sec. 7.6). Leveraging the diverse synthetic dataset and high-fidelity reconstructions, `MagLens` can also infer material degradation severity, such as rebar corrosion (Sec. 7.5).

We evaluate `MagLens` across diverse scenarios, covering representative ferrous building components including rebars, metal studs,

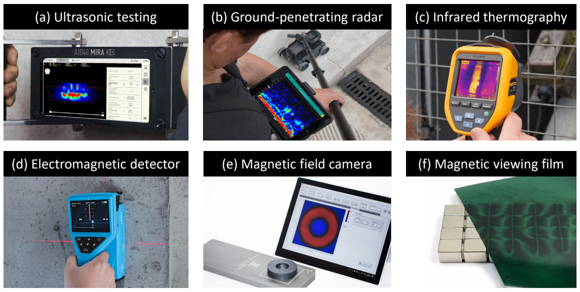

Figure 2: Non-destructive inspection techniques [15, 20, 22, 27] and magnetic visualization tools [17, 19].

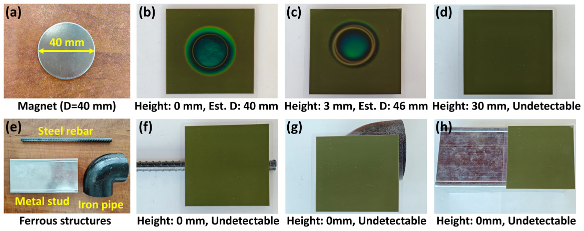

Figure 3: Magnetic field visualization using viewing film. The magnet contour disappears beyond 3 cm, and ferrous structures remain invisible even at 0 cm.

and iron pipes. We assess `MagLens`' ability to reconstruct rebar contours under varying distances, orientations, spatial positions, and structural layouts such as bent segments and multi-rebar configurations. By leveraging the reconstructed contours, one can estimate material loss from contour deformation and cross-sectional narrowing [56], thus enabling corrosion inference. Our experiment on a custom-built wall shows that `MagLens` can merge multiple scans into a global reconstruction, demonstrating the mobility and usability of the handheld form factor (Fig. 1(a)). We also evaluate imaging stability under varying magnetization states and assess generalization to ferrous objects *not seen* during the training phase. We further demonstrate the efficacy of our physics-informed synthesis, resilience to in-wall EMI interference [68, 90], and contour reconstruction of rebars in real walls. We also analyze the power consumption and the inference latency. Together, these results prove `MagLens`' unique advantage in mobility, accuracy, and practicality for ferrous structure inspection.

In summary, this paper makes the following contributions:

- A synthetic aperture-based scanning mechanism that enables high-fidelity magnetic field acquisition using a compact and cost-efficient magnetometer array;
- A physics-informed imaging pipeline trained on synthesized magnetic field data;
- Extensive real-world evaluations across diverse ferrous structures and deployment scenarios.

2 Background and Motivation

2.1 Ferrous Structure Inspection

After the Surfside collapse, the Florida Milestone Inspection Law [12] and NYC Local Law 11 [26] mandated recurring inspections of buildings, façades, and exposed steel. Of these inspections, the health of ferrous structures is of paramount importance because (1) steel is fundamental to the structural integrity, and (2) if neglected, anomalies such as bending or corrosion propagate rapidly and compromise safety. The risks are further amplified in harsh environments, such as coastal regions, where chloride ingress and moisture accelerate corrosion and structural deterioration [31]. Therefore, accurate inspection of the position, layout, and degradation of ferrous structures is essential for failure prevention.

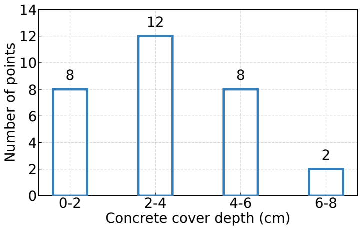

Figure 4: Distribution of real-world rebar cover depths.

Existing inspection techniques are divided into two categories: destructive and non-destructive methods. Destructive approaches, such as core drilling and electrochemical tests [53, 61, 64, 66], require direct access to internal ferrous components. This exposure enables direct measurement of corrosion potential, cross-sectional loss, and other structural damage indicators. However, these methods are labor-intensive and compromise the structural integrity. Non-destructive techniques include ultrasonic testing, GPR, infrared thermography, and electromagnetic detectors (Figs. 2(a)–(d)). Ultrasonic methods assess material continuity and detect delamination, but require direct contact and are sensitive to surface conditions. GPR enables subsurface sensing by analyzing reflected electromagnetic waves. However, its long wavelength limits resolution, causing objects smaller than 2 inches (5 cm) to appear as indistinct "dots" [5, 76]. Infrared thermography reveals surface temperature variations but is limited to shallow anomalies and sensitive to environmental conditions. Electromagnetic detectors, such as handheld rebar locators, infer the presence and depth of metallic objects from magnetic permeability. However, their accuracy is constrained by environmental interference, with diameter deviations up to 19 mm and cover depth errors of 14–31% [79].

2.2 Primer of Magnetic Sensing

2.2.1 Magnetic visualization techniques. Magnetic visualization methods leverage the field perturbations induced by ferrous objects and can be categorized into active sensor arrays [67, 84] and passive magnetic viewing films [4]. Sensor arrays provide high-resolution field mapping but require dense, static deployment and millimeter-level proximity to the target (Fig. 2(e)), making them impractical for mobile inspections. Magnetic viewing films offer a low-cost visual alternative (Fig. 2(f)) but suffer from short sensing ranges and coarse resolution. To illustrate these limitations, we used magnetic viewing film to visualize the field of a 40 mm cylindrical magnet at varying distances. As shown in Figs. 3(b)–(d), the magnet's field is clearly visible at direct contact (i.e., 0 cm), becomes faint at 3 mm, and disappears entirely beyond 30 mm, despite the magnetic field at that distance exceeding 7,200 μT. In comparison, ferrous structures such as rebars generate fields of only 25 μT at the same distance (Sec. 4.1). Furthermore, real-world ferrous structures are typically embedded much deeper. According to the American Concrete Institute (ACI),

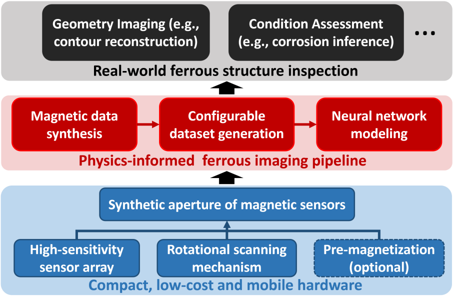

Figure 5: System overview of `MagLens`.

concrete cover depths for rebars typically range from 2 to 7 cm [10]. We also surveyed 30 structural sites (e.g., walls, staircases, columns) using a rebar locator. As shown in Fig. 4, 22 of the 30 rebars are embedded deeper than 2 cm beneath the surface, which exceeds the effective range of existing magnetic visualization methods.

2.2.2 Ferromagnetism in structural materials. Ferrous materials consist of microscopic magnetic domains that align under an external magnetic field [2, 23]. Due to hysteresis [46], this alignment partially persists after field removal. In practice, manufacturing processes such as quenching, forging, and cutting expose ferrous structures (e.g., rebars) to strong magnetic fields, resulting in residual magnetization [54]. This remanence is stable because concrete is non-magnetic and building environments contain no strong static perturbations [35]. According to [46], ferrous materials would be *demagnetized* after passing their Curie temperature — 770 °C for iron alloy. However, the remanent fields are *orders of magnitude* weaker than those of magnets. As demonstrated in Figs. 3(f)–(h), magnetic viewing film fails to reveal discernible contours even at direct contact. As we will elaborate in Sec. 4.1, the magnetic field of a metal stud drops below 10 μT at a distance of 5 cm. To detect such weak signatures, prior solutions such as iCAMM [21] and IGS [28] employ high-sensitivity sensors to capture field distributions for structural anomaly detection within a range of up to 10 cm. However, iCAMM falls short in the localization capability, thus requiring a rebar locator to determine position and depth prior to the scanning procedure [75]. IGS system is confined to rebar deterioration diagnosis and cannot inspect other ferrous structures, limiting its applicability to broader inspection tasks. Both systems produce only vague magnetic anomaly *heatmaps* without fine-grained geometric attributes (e.g., contour, diameter). Thus, we ask a key question: *Can we achieve fine-grained inspection of key factors including contour, depth, and material condition (e.g., corrosion) of ferrous structures using a low-cost, mobile sensing system?*

3 Overview of `MagLens`

`MagLens` aims to provide fine-grained imaging of ferrous objects for detecting geometric features and structural deterioration (e.g., corrosion). Unlike prior methods that output field maps or coarse indications, `MagLens` reconstructs *object contours* and *cover depth* via a lightweight neural-network-based inverse mapping. It offers three key capabilities over existing methods: (1) detection of weak magnetic signatures at practical concrete cover depths (i.e., several centimeters beneath the concrete surface [10]); (2) collection of spatially dense measurements via a portable hardware design; and (3) reconstruction of key structural attributes, including contours and depths, with a lightweight, learning-based imaging pipeline. Fig. 5 presents an overview of `MagLens`. The hardware (Sec. 4) integrates a high-sensitivity sensor array, a rotational scanning mechanism, and an optional pre-magnetization module. The imaging pipeline (Sec. 5) comprises magnetic data synthesis, configurable dataset generation, and neural network modeling.

4 Synthetic Aperture of Magnetic Sensors

4.1 High-sensitivity Sensor Array

Prior magnetic sensing systems [42, 44, 45] often employ low-cost Hall-effect sensors. However, their limited sensitivity, thermal drift, and inherent bias [89] hinder reliable detection of weak magnetic signatures. To address these limitations, `MagLens` uses the magneto-inductive RM3100 (Fig. 6(a)). Fig. 7(a) compares static readings from RM3100 and a Hall-effect sensor (MLX90393 [13]) under identical settings. The (mean, STD) of RM3100 and MLX90393 are (39.08 μT, 0.06 μT) and (61.21 μT, 1.21 μT). The offset and higher noise level in MLX90393 indicate the intrinsic bias and lower stability of COTS Hall-effect sensors. In contrast, RM3100 delivers bias-free measurements across sensors, as its magneto-inductive principle eliminates static offsets by measuring changes in magnetic flux.

To assess the magnetic field strength of real-world ferrous structures, we measured three common building components *without external magnetization* using a single RM3100 sensor: a steel rebar, a metal stud, and a cast iron pipe (Fig. 3(e)). Each object was centered beneath the sensor, and static magnetic field readings were collected at distances ranging from 1 cm to 11 cm. The object-induced field was computed by subtracting the background geomagnetic field measured under identical conditions without the object. As shown in Fig. 7(b), all three objects exhibit weak magnetic signatures that decay rapidly with distance. For example, the field from the metal stud drops below 10 μT at 5 cm, which is significantly lower than the geomagnetic field measured at the site (i.e., 39 μT). These results confirm that ferrous structures generate weak magnetic fields at practical sensing distances.

After sensor selection, we co-design the array geometry and sampling density to reliably capture weak remanence under a compact form factor. Existing dense 2D grids incur increased hardware complexity, high power consumption, and reduced mobility. In contrast, `MagLens` adopts a lightweight linear array to minimize system overhead. As shown in Fig. 6(a), our prototype comprises nine RM3100 sensors with 2 cm spacing, which accommodates the RM3100 packaging while preserving sufficient aperture length for coverage. Combined with rotational scanning (Sec. 4.2), this co-design achieves high angular sampling density and broad spatial coverage without requiring a large number of sensors.

4.2 Rotational Scanning Mechanism

To enable wide-area magnetic field acquisition with minimal hardware, `MagLens` employs a rotational scanning mechanism inspired by SAR [73]. Unlike SAR, `MagLens` measures static remanent fields and does not use phase-coherent reconstruction. Compared to conventional linear scanning, rotation ensures uniform and repeatable spatial sampling, mitigating motion-induced errors such as speed variation and angular drift. It also extends sensing coverage without

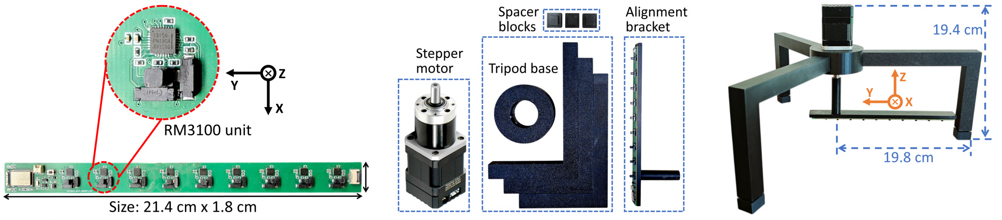

(a) Compact magnetic sensor array (b) Motor and fixture components (c) Assembled scanning platform

Figure 6: Hardware design of `MagLens`. The mobile form factor only weighs 922.4 g, enhancing `MagLens`' portability.

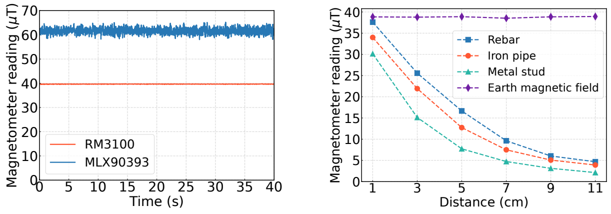

(a) RM3100 vs. MLX90393 (b) Readings w/ varying distances

Figure 7: Raw data of magnetometers.

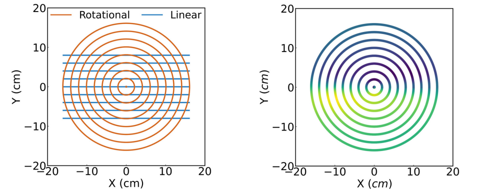

(a) Scanning trajectories (b) Raw measurements (x-axis)

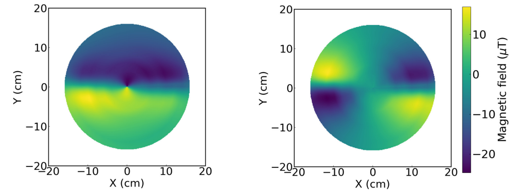

(c) Interpolated field map (d) Compensated field map

Figure 8: Scanning patterns and rotation compensation.

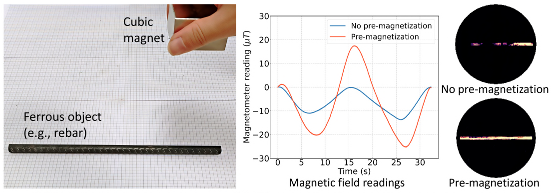

(a) Pre-magnetization setup (b) Effect on signal strength and contour reconstruction

Figure 9: Pre-magnetization for long-range imaging.

requiring additional sensors. As illustrated in Fig. 8(a), rotating the sensor array along a 16 cm radius covers 804 cm^2 ($\pi \cdot 16^2$), compared to 512 cm^2 for a 32 cm linear path. This corresponds to a 1.57× improvement in spatial coverage at equal hardware cost.

4.2.1 High-precision rotational control. `MagLens` employs a high-precision rotational mechanism driven by a stepper motor (Fig. 6(b)). The motor provides sub-degree angular steps with closed-loop feedback, ensuring precise and uniform rotation. The system allows *configurable* rotation speeds, with a default setting of 10°/s. A modular 3D-printed fixture rigidly couples the sensor array to the motor shaft while preserving portability and mechanical stability. As shown in Fig. 6(b), the fixture integrates a tripod base for structural support, an alignment bracket for sensor array centering, and stackable spacer blocks to adjust sensing distance. The fully assembled platform, i.e., Fig. 6(c), is compact and lightweight, measuring 19.8 cm in radius and 19.4 cm in height, enabling rapid deployment.

4.2.2 Data interpolation. Rotational scanning improves spatial coverage but introduces two key challenges. First, sensors at different radii have varying linear velocities, resulting in non-uniform sample spacing. Second, measurements are confined to discrete rings, leaving gaps between adjacent sensing paths (Fig. 8(b)). To address both issues, `MagLens` employs a lightweight interpolation module that reconstructs a dense and uniform magnetic field map from sparse measurements. Specifically, `MagLens` applies nearest-neighbor interpolation [85] to estimate values at unmeasured locations. As shown in Fig. 8(c), rotational samples are interpolated onto a uniform grid, producing a continuous field representation.

4.2.3 Rotation compensation. Preserving the correct orientation of magnetic vectors after interpolation is critical for spatial consistency. The array is mounted with the z-axis perpendicular to the rotation plane and the x-y axes aligned with the plane (Fig. 6(c)). We denote the tri-axial magnetic field measured by the array as $\mathbf{B} = [B_x, B_y, B_z]$. This setup ensures that B_z remains invariant to sensor rotation. However, the in-plane components (B_x, B_y) rotate with the array, introducing angle-dependent distortions even in static fields. As shown in Fig. 8(c), the interpolated B_x map exhibits periodic artifacts that obscure the object's geometry. To correct for these distortions, `MagLens` performs real-time rotation compensation. During scanning, the array rotates clockwise with angular velocity ω. The instantaneous rotation angle is computed as $\theta = \omega t$, where t denotes the elapsed time since the scan began. Each in-plane magnetic vector (B_x, B_y) is then transformed into the global coordinate frame aligned with the array's initial orientation (i.e., 0°) as shown in Fig. 6(c)), using:

$$\begin{aligned} B_x' &= B_x \cos\theta + B_y \sin\theta, \\ B_y' &= -B_x \sin\theta + B_y \cos\theta. \end{aligned} \tag{1}$$

This transformation eliminates orientation-induced fluctuations. As shown in Fig. 8(d), the compensated B_x field map reveals distinct object-specific patterns of the rebar.

4.3 Optional Pre-magnetization Module

`MagLens`' hardware design enables high-fidelity magnetic field acquisition at typical cover depths (e.g., 5 cm). However, at longer ranges, the cubic decay of magnetic field severely weakens the

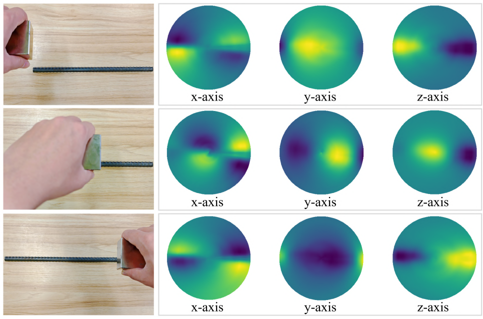

Figure 10: Field patterns under different magnet placements.

signal. Fig. 9(b) shows that a scan at 11 cm produces weak measurements and incomplete contour reconstruction. To extend the effective sensing range without increasing hardware complexity, `MagLens` introduces an *optional pre-magnetization step* as shown in Fig. 9(a). Before the scanning procedure, the user can briefly position a passive magnet above the target (typically for 1–2 s) to induce magnetization. In real deployments, this is typically performed by placing the magnet directly against the wall surface, which remains effective since concrete is non-ferromagnetic (Sec. 7.9). Our prototype employs a 5×5×3 cm^3 N52-grade cubic magnet, with its N/S poles oriented toward the ferrous target to maximize magnetization. As shown in Fig. 9(b), this short exposure enhances field intensity and contour reconstruction performance even at 11 cm.

The induced field pattern depends on the magnet's orientation and placement, even for the same target. We magnetize the same rebar at three locations (left/middle/right) at a height of 11 cm and measure the tri-axial magnetic field. As shown in Fig. 10, pre-magnetization at all three positions is effective. However, the resulting patterns vary with magnet placement, posing a challenge for consistent imaging. To decouple geometry from magnetization, we introduce a physics-informed data synthesis that simulates diverse magnetization parameters on fixed geometry (Sec. 5.2).

5 Physics-informed Imaging Pipeline

5.1 Magnetic Data Synthesis

5.1.1 Physics-informed data synthesis. Collecting large-scale magnetic field measurements is costly, labor-intensive, and difficult to scale across diverse conditions. To address these difficulties, `MagLens` generates labeled training data by simulating the magnetic fields induced by ferrous structures, which exhibit spatial patterns characteristic of magnetic dipoles [63]. While finite element analysis (FEA) [94] can model such patterns, it is computationally expensive and requires expert parameter tuning, making it impractical for large-scale data synthesis. Instead, `MagLens` employs an efficient permanent magnet–based approximation that preserves key physical properties while reducing computational cost.

5.1.2 Voxelized magnet modeling. A common simplification is to model a ferrous structure as a single magnet, e.g., a rebar as a cylindrical magnet or an iron pipe as a ring dipole using simulation tools such as Magpylib [78]. However, this approach produces *oversimplified* field patterns. As shown in Fig. 11(b), a cylindrical magnet generates end-concentrated fields with a sharp drop in the center. In contrast, measurements from real rebars (Fig. 11(a)) reveal smooth and continuous distributions along the entire length. These discrepancies indicate that the single-magnet approximation fails to capture the spatial characteristics of real-world ferrous structures.

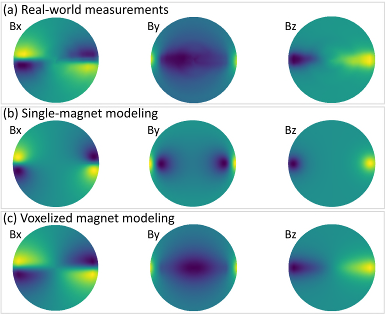

Figure 11: Magnetic field distributions of a rebar.

To bridge this gap, `MagLens` adopts a *voxelized magnet model*, which decomposes each ferrous object into a series of discretized, magnetized segments, implemented using Magpylib and standard discretization in field computation [60]. This design is physically motivated by the internal structure of ferrous materials, which consists of numerous locally magnetized domains [23]. By modeling each voxel as an independent magnetic dipole with appropriate strength and orientation, the aggregated field accurately captures the spatially distributed behavior of ferrous objects. To reflect the smooth field distributions observed in real measurements (Fig. 11(a)), `MagLens` applies a spatially weighted voxel magnetization scheme following a Gaussian profile:

$$M(i) = M_0 \cdot \exp\left(-\frac{(i - N/2)^2}{2\sigma^2}\right), \tag{2}$$

where M_0 denotes the peak magnetization at the object center, N is the total number of voxels, i is the voxel index, and σ controls the spread of the magnetization. With voxel modeling, the model produces magnetic field patterns that closely match experimental observations, as shown in Fig. 11(c).

5.1.3 Automated data synthesis. To enable scalable data generation, `MagLens` implements an automated pipeline that synthesizes triaxial magnetic fields directly from 3D object geometries. As shown in Fig. 12(a), the pipeline only requires basic size parameters as input. Note that these parameters are easy to obtain via measurement or 3D reconstruction methods such as photogrammetry [59]. Given the input, the pipeline voxelizes the geometry (Fig. 12(b)) and then simulates the magnetic fields. As shown in Fig. 12(c), the synthesized maps exhibit consistent alignment with real measurements.

5.2 Configurable Dataset Generation

`MagLens` constructs a scalable dataset comprising diverse synthetic samples, a small real-world subset, and dual labels for contour and depth. The overall composition is summarized in Table 1. The synthetic set includes single-object samples (rebar, iron pipe, metal stud) to ensure type diversity, and multi-object layouts capturing practical rebar assemblies. To mitigate domain shift, we fine-tune on 720 real rebar samples, a scale consistent with prior studies showing that 1–3% labeled target data is sufficient for effective adaptation [43, 71], as demonstrated in Sec. 7.6.

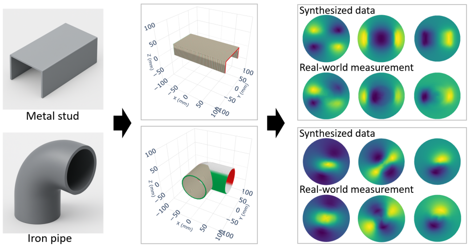

(a) Object geometries (b) Voxelized modeling (c) Synthesized vs. real magnetic fields

Figure 12: Synthesis pipeline for ferrous structures.

Table 1: Dataset composition of `MagLens`.

Subset	Configuration	Samples
Synthesized (single-object)	$64 \times 12 \times 3 \times 3 \times 3$	20,736 (76.0%)
Synthesized (multi-object)	$18 \times 12 \times 3 \times 3 \times 3$	5,832 (21.4%)
Real-world	$10 \times 12 \times 6$	720 (2.6%)
Total	–	**27,288**

Table 2: Object geometry configurations.

Object type (Geometry)	Parameter values (Unit: mm)	Instances
Rebar (Straight)	Diameter:{6, 12, 18, 24}; Length:{100, 200, 300, 400}	16
Rebar (Bent)	Diameter:{6, 12, 18}; Length:{100, 300}; Angle:{45°, 90°}	12
Iron pipe (Straight/Elbow)	Outer diameter:{30, 60, 90, 120}; Wall thickness:{2, 8}	16
Metal stud (C-shaped)	Web:{30, 50, 70, 90, 110}; Flange:{10, 20, 30, 40}; Length:150	20
Total	–	**64**

5.2.1 Variation factors. We synthesize 26,568 samples by systematically varying object geometry, sensing distance, magnetization, multi-object layout, and placement.

Object geometry. We model three representative ferrous objects: cylindrical rebars, hollow iron pipes, and C-shaped metal studs. Each type spans realistic structural dimensions observed in built environments. To further diversify field patterns, we include bent rebars and elbow pipes with 45° and 90° angles. As summarized in Table 2, this design yields 64 object geometries.

Sensor-target distance. We vary sensing distance from 10 mm to 120 mm in 10 mm increments, covering 12 levels. This range is consistent with typical cover depths (i.e., 2–7 cm in [10]) and the effective sensing range (up to 10 cm) of existing inspection systems [21, 28]. Such a design enables the model to learn distance-aware features and maintain robustness across different depths.

Magnetization configuration. To decouple the geometric pattern from magnetization state, for each object, we sample three magnetization orientations along the 3D axes (x, y, z), which helps capture alignment uncertainty. We also set magnitudes to three levels to emulate variations in strength (e.g., due to different ferrous materials). This configuration enables consistent reconstruction across different magnetization states (Sec. 7.4).

Multi-object layout. Structural codes [10, 16] specify that residential walls use either a single rebar mesh or two meshes near opposite faces, with typical inter-layer spacing of 80–120 mm. Within each layer, rebars are arranged in parallel or orthogonal patterns with 50–150 mm spacing [8]. Based on these standards, we design 18 representative layouts covering single- and double-layer meshes with aligned and orthogonal combinations, enabling the model to disentangle contours in densely reinforced environments (Sec. 7.9).

Object placement. By default, the target is placed horizontally with its geometric center aligned to the rotation center (Fig. 6(c)). To simulate realistic misalignment, we additionally shift the target within the scanning plane: a 5 cm displacement along the x-axis and another along the y-axis.

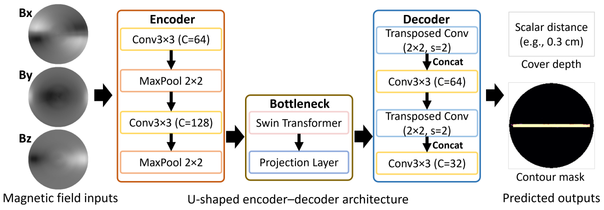

Figure 13: The imaging architecture of `MagLens`.

5.2.2 Real-data integration. To bridge the domain gap between simulated and real-world data (Fig. 12(c)), `MagLens` incorporates a small real-world subset. It comprises measurements from ten HRB400-grade rebars of varying diameters and lengths, collected under the controlled setup in Fig. 14(a) with known geometry and distance. Each specimen is scanned across 12 sensing distances and six magnetization configurations, producing 720 samples in total.

5.2.3 Label design. Each sample is annotated with two labels: *(i)* a pixel-level binary contour mask (1 for object region, 0 otherwise) representing the object's footprint on the xy-plane, and *(ii)* a scalar indicating the vertical distance between the sensor and the object.

Distance-aware contour scaling. Using a fixed contour mask across all sensing distances neglects the depth-dependent variation in the magnetic field distribution. For example, scanning a rebar at 1 cm and 5 cm yields the same ground-truth contour, providing no depth-specific supervision and hindering the learning of distance-aware features. To address this, `MagLens` scales the contour mask with sensing distance, modestly enlarging it at greater depths to reflect weaker, more diffuse fields. Specifically, we adopt a logarithmic scaling function rather than a linear one to avoid excessive expansion for elongated objects (e.g., rebars) at far ranges. Given a reference distance d_0, the scaling factor for distance d is:

$$s = \frac{\log(d + k)}{\log(d_0 + k)}, \tag{3}$$

where k is a smoothing constant that stabilizes the scaling function at short ranges. During inference, the predicted depth is used to rescale the mask to its true spatial size.

5.3 Neural Network Modeling

`MagLens` employs a hybrid CNN–Transformer architecture with dual outputs to jointly predict the contour and depth of ferrous structures. The model follows a U-shaped encoder–decoder design with a Swin Transformer [40] bottleneck and two task-specific output heads (Fig. 13). We normalize each sample's field pattern to eliminate amplitude scaling and offset. The input is a 256×256×3 field map comprising B_x, B_y, and B_z channels. The encoder extracts low-level features via two 3×3 convolutional layers, interleaved with two 2×2 max-pooling layers. The Swin Transformer bottleneck applies windowed self-attention over the 64×64 feature map to capture long-range spatial dependencies. The decoder upsamples features through two transposed convolution layers and concatenates them with encoder features at corresponding resolutions. Two task-specific heads operate on the final feature map. The segmentation head uses a 1×1 convolution and sigmoid activation to produce a contour mask. The regression head estimates the sensor–object distance. We train the network using a weighted multi-task loss:

$$\mathcal{L}_{\text{total}} = \mathcal{L}_{\text{mask}} + \lambda \cdot \mathcal{L}_{\text{dist}}, \tag{4}$$

where λ balances the segmentation and distance regression tasks. The segmentation loss $\mathcal{L}_{\text{mask}}$ is a compound objective:

$$\mathcal{L}_{\text{mask}} = \lambda_{\text{FT}} \cdot \mathcal{L}_{\text{FT}} + \lambda_{\text{Dice}} \cdot \mathcal{L}_{\text{Dice}}. \tag{5}$$

Here, $\mathcal{L}_{\text{FT}}$ denotes the Focal Tversky loss [32], designed to address foreground–background imbalance and subtle boundaries. This is critical in our setting, where foreground regions (e.g., thin rebar) typically occupy $< 5\%$ of the image. $\mathcal{L}_{\text{Dice}}$ complements this by maximizing global shape overlap [72], thus improving contour coherence. For distance regression, we apply mean squared error:

$$\mathcal{L}_{\text{dist}} = \left\| d_{\text{pred}} - d_{\text{true}} \right\|_2^2, \tag{6}$$

where d_{true} is the ground-truth sensor–object distance.

6 System Implementation

6.1 Hardware Implementation

Sensor array. Each RM3100 sensor operates at a cycle count of 200, achieving a sampling rate of 60 Hz with high sensitivity. Magnetic readings are collected via a 1 MHz SPI bus [1] and processed by an MDBT42Q-512KV2 Bluetooth Low Energy (BLE) module [6], which integrates an nRF52832 SoC for real-time data aggregation and wireless transmission. Synchronized readings are streamed to a host device (e.g., laptop) over BLE. The sensor array is powered by a 3.7 V, 200 mAh lithium-polymer (Li-Po) battery, enabling untethered operation. The total hardware cost is less than $150.

Mechanical rotation unit. The stepper motor provides a step angle of 0.13°. An onboard STM32F103C8T6 microcontroller [30] autonomously executes a predefined rotation sequence upon power-up, enabling fully standalone operation without host control. The rotation speed is *configurable*, with a default of 10°/s. The motor is powered by a 12 V, 2,000 mAh Li-Po battery. The rotation unit, including motor and battery, costs less than $40. The complete assembly weighs 922.4 g and supports portable operation.

6.2 Dataset and Network Configuration

Dataset. For data synthesis, the voxel count N is set to twice the object length with a Gaussian spread $\sigma = 0.38$. Contour scaling uses a reference distance $d_0 = 3$ cm and smoothing constant $k = 5$. The pipeline generates each sample in about 0.88 s using a laptop (Intel i7-1260P, 16 GB RAM). All images are normalized to zero mean and unit variance, and distance values are scaled to the $[0, 1]$ range.

Network configuration. For training, the distance regression loss is weighted by $\lambda = 0.2$. The segmentation loss is a combination of Focal Tversky ($\lambda_{\text{FT}} = 0.7$) and Dice ($\lambda_{\text{Dice}} = 0.3$). We adopt the Adam optimizer with an initial learning rate of 1×10^{-3} and a weight decay of 1×10^{-5}, applying gradient clipping with a maximum norm of 1.0. The learning rate is reduced by 0.5 when validation loss plateaus for 10 epochs. Training runs for 100 epochs with a batch size of 8, implemented in PyTorch 2.4.1 and Python 3.12 on an NVIDIA RTX 3090 GPU. The model is then fine-tuned on the real subset. During this phase, the encoder and Transformer bottleneck are frozen, while the decoder and output heads are updated for 30 epochs using a learning rate of 5×10^{-5} and a batch size of 4.

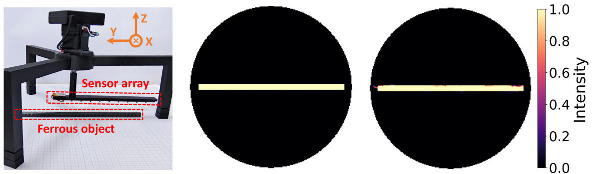

(a) Experimental setup (b) Ground-truth contour (c) Predicted imaging result

Figure 14: The setup and imaging result illustration.

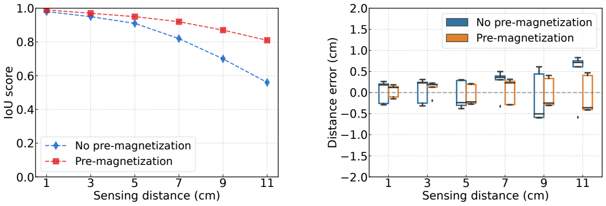

(a) IoU score (b) Distance error

Figure 15: The impact of varying distances.

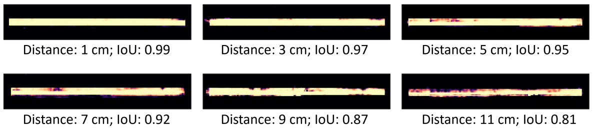

Figure 16: Imaging results of varying distances.

7 Evaluation

7.1 Experimental Settings

Fig. 14(a) shows the setup. All samples are placed on 1 mm-resolution graph paper for precise spatial alignment. We derive ground-truth contour masks based on known geometry parameters. For irregular geometries (e.g., garden shears), we use manufacturer specifications and available CAD files. Giving these inputs and the relative position between the sensor array and the target, we can obtain the 2D contour. Depth is defined as the vertical distance from the sensor array to the object surface and is measured with a vernier caliper. The default model is fine-tuned with 720 real samples.

We first evaluate `MagLens` on HRB400-grade rebars (12 mm in diameter, 30 cm in length) without external magnetization, covering variations in depth, diameter, spatial and angular offsets, multi-object layouts, and rotation speeds. All rebar evaluation data are collected on rebar specimens distinct from the ten rebars used in the fine-tuning subset. Each configuration is repeated five times. By default, the sensor array is placed 3 cm above the target, reflecting the real-world cover depths as shown in Sec. 2.2. We further extend the distance up to 11 cm in Sec. 7.3.1. For usability, we scan rebars with different corrosion levels to evaluate `MagLens`' sensitivity to millimeter-scale cross-sectional loss, and validate end-to-end performance using a handheld scan of a wall testbed. We also evaluate `MagLens` on metal studs, iron pipes and irregular objects (e.g., garden shears), resilience to in-wall electrical cables, and measure the power consumption and inference latency.

7.2 Evaluation Metrics

`MagLens` outputs a normalized contour probability map, where each pixel denotes the likelihood of belonging to the object region (0

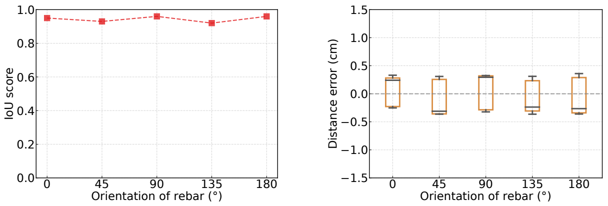

(a) IoU score (b) Distance error

Figure 17: The impact of varying orientations.

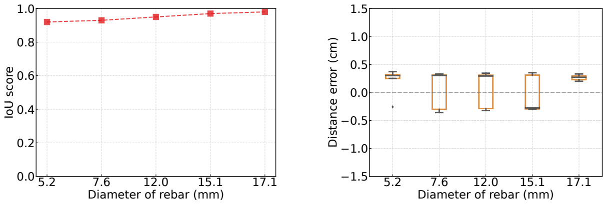

(a) IoU score (b) Distance error

Figure 18: The impact of varying diameters.

for background, 1 for contour). Fig. 14(b) shows the ground-truth contour mask, and Fig. 14(c) presents a sample prediction. These contour maps visualize ferrous structures and reveal geometry, orientation, and material degradation such as corrosion-induced contour distortion. To quantify reconstruction accuracy, we binarize the predicted map at a 0.5 threshold and compute the Intersection over Union (IoU) with the ground truth A_{gt}:

$$IoU = \frac{A_{pred} \cap A_{gt}}{A_{pred} \cup A_{gt}}, \tag{7}$$

where higher IoU indicates better contour alignment. The depth estimation accuracy is reported as the relative error between prediction $\hat{d}$ and ground truth d, i.e., $\hat{d} - d$.

7.3 Geometry Imaging Performance

7.3.1 Varying sensing distances. We evaluate `MagLens` at sensing distances from 1 cm to 11 cm in 2 cm increments, under two settings: (i) a rebar without external magnetization, and (ii) the same rebar after pre-magnetization at 11 cm (Sec. 4.3). As shown in Fig. 15, `MagLens` achieves high accuracy under the default setting, with IoU scores of 0.98, 0.95, and 0.91 at 1 cm, 3 cm, and 5 cm and distance errors of 0.24 cm, 0.26 cm, and 0.30 cm, respectively. These results indicate reliable reconstruction at typical cover depths. Beyond 5 cm, performance degrades due to the cubic decay of magnetic field, with IoU dropping to 0.56 and distance error rising to 0.82 cm at 11 cm. Pre-magnetization effectively enhances reconstruction accuracy at extended sensing distances. Specifically, at 9 cm and 11 cm, IoU increases from 0.70 to 0.87 and from 0.56 to 0.81, corresponding to relative gains of 24.3% and 44.6%. Distance errors remain below 0.5 cm across all depths. Fig. 16 visualizes the raw contour probability map and demonstrates consistent reconstruction with pre-magnetization. In practice, one can perform a standard scan first and enable pre-magnetization when the measured field signatures are weak and the reconstruction is incomplete.

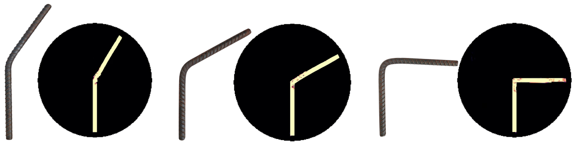

(a) Bending angle: 30° (b) Bending angle: 60° (c) Bending angle: 90°

Figure 19: Imaging results of bent rebars.

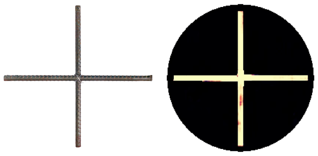

Figure 20: Imaging results of intersecting rebars.

7.3.2 Varying rebar orientations. We now assess `MagLens`' robustness to diverse object orientations. The default orientation (i.e., 0°) aligns the rebar with the sensor's y-axis. We rotate the rebar counterclockwise to different orientations, including 45°, 90°, 135°, and 180°. As shown in Fig. 17, `MagLens` achieves high IoU across all angles, with scores of 0.95, 0.93, 0.96, 0.92, and 0.96, respectively. The (mean, STD) of the distance error is (0.31 cm, 0.04 cm).

7.3.3 Varying rebar diameters. We evaluate `MagLens` on rebars with diameters of 5.2 mm, 7.6 mm, 12.0 mm, 15.1 mm, and 17.1 mm to reflect dimensional variability. As shown in Fig. 18(a), average IoU scores range from 0.92 to 0.98. Distance errors remain below 0.4 cm across all sizes, including the thinnest 5.2 mm rebar (Fig. 18(b)).

7.3.4 Varying rebar positions. To assess `MagLens`' resilience to target misalignment, we introduce two spatial offsets between the rebar and the sensor array. Specifically, the rebar is shifted by 5 cm and 10 cm along the x-axis to emulate off-center placement. `MagLens` maintains reliable performance, achieving IoU scores of 0.93 and 0.88 with corresponding distance errors of 0.29 cm and 0.35 cm. The slight degradation at 10 cm is attributed to the weaker signals near the scan boundary. In practice, `MagLens`' handheld design and real-time feedback allow users to reorient the device and re-center the region of interest (ROI) for improved accuracy. We demonstrate this usage model in Sec. 7.9.

7.3.5 Bent rebars. We evaluate `MagLens`' ability to reconstruct non-linear geometries such as bent rebars. Such bends may be intentional in design (e.g., rebar stirrups) or arise from long-term stress-induced deformation. We test three rebars bent at 30°, 60°, and 90°, where the 30° and 60° are *unseen* during training. As shown in Fig. 19, `MagLens` reconstructs all three shapes with IoU scores of 0.92, 0.94, and 0.88, respectively. The distance errors remain below 0.37 cm. The 90° sample exhibits slightly lower accuracy due to magnetic field distortion at sharp bends.

7.3.6 Intersecting rebars. Reinforced structures often contain intersecting rebars [8]. We evaluate this scenario using two 30 cm rebars placed at a 90° angle. As shown in Fig. 20, `MagLens` reconstructs the geometry of both rebars with high fidelity, achieving an IoU of 0.96 and a maximum distance error of 0.28 cm, demonstrating robustness to multi-source magnetic field superposition [63]. This resilience is enabled by our synthetic dataset, which includes diverse multi-layout configurations. We also assess performance on parallel layouts during the end-to-end scanning in Sec. 7.9.

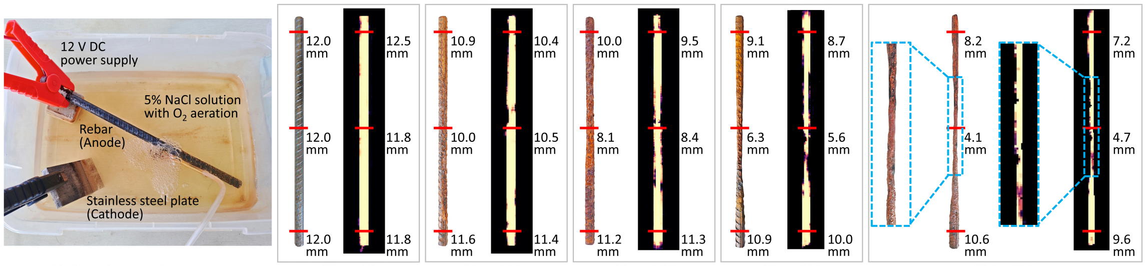

(a) Corrosion experiment setup (b) t = 0 h (c) t = 18 h (d) t = 36 h (e) t = 54 h (f) t = 72 h

Figure 21: Corrosion setup and imaging results of the rebar at different corrosion levels.

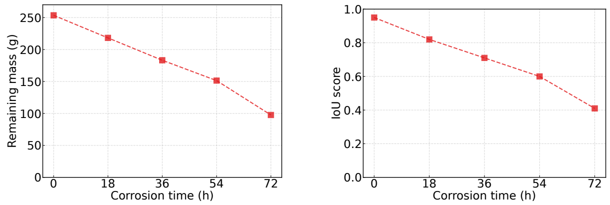

(a) Remaining mass (b) IoU score

Figure 22: Results under different corrosion levels.

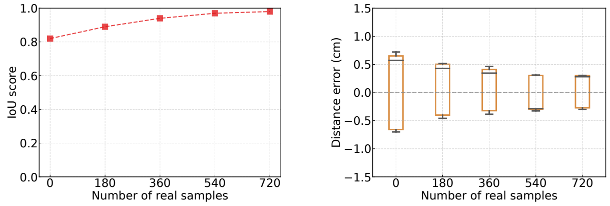

(a) IoU score (b) Distance error

Figure 23: The impact of the number of real samples.

7.3.7 Varying rotational speeds. The rotational speed directly affects the scan duration and temporal resolution. To assess this impact, we evaluate `MagLens` at 20°/s, 30°/s, and 60°/s. Across these settings, the system delivers high accuracy, with IoU scores of 0.94, 0.91, and 0.84, and distance errors of 0.26 cm, 0.33 cm, and 0.38 cm, respectively. Note that, at 60°/s, a full scan is completed in only six seconds, enabling rapid operation in time-sensitive scenarios without significant performance degradation.

7.4 Stability under Varying Magnetization

To assess the stability of `MagLens`’ contour reconstruction under varying magnetization, we fix geometry and vary magnetization placement. Specifically, we use the HRB400-grade rebar and pre-magnetize it at three positions along the bar (left/middle/right) at 5 cm depth following Sec. 4.3. Across these conditions, `MagLens` reconstructs consistent contours, achieving IoUs of 0.94, 0.96, and 0.94, with depth error below 0.35 cm.

7.5 Corrosion Level Inference

To emulate long-term corrosion in reinforced concrete, we employ a constant-current electrochemical acceleration protocol used in structural durability studies [58, 92]. As shown in Fig. 21(a), the rebar specimen immersed in a 5% NaCl electrolyte and subjected to a DC current to induce anodic dissolution over five exposure intervals (0, 18, 36, 54, and 72 hours). Oxygen aeration is used to accelerate the corrosion. We employ two metrics as ground truth: (i) remaining mass [34, 81] and (ii) cross-sectional diameter reduction [56]. After each interval, the specimen is cleaned, dried, and weighed following a standardized procedure [77]. Diameter reduction is recorded with precision calipers at three axial positions.

(a) Galvanized metal stud (b) Cast iron pipe elbows

Figure 24: Imaging results for metal studs and iron pipes.

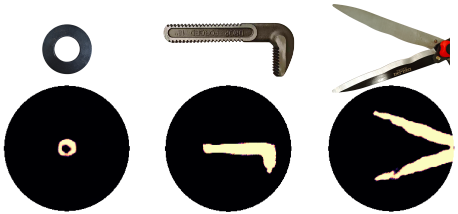

(a) Disc spring (b) Pipe-wrench hook jaw (c) Garden shears

Figure 25: Imaging results for unseen ferrous objects.

Figs. 21(b)–(f) shows the side-by-side comparisons of physical samples and reconstructed contours at each time point. Diameters at three locations are estimated from the predicted contours via pixel-to-metric scaling. The maximum estimation error is 1 mm, observed at the most severely corroded stage (t=72 h), indicating that `MagLens` can resolve millimeter-scale geometric loss. To quantify contour degradation, we compute the IoU between each predicted contour and the ground-truth mask at t=0 h. As shown in Fig. 22, both IoU and the measured remaining mass decline consistently over time, confirming that `MagLens` captures material loss and that IoU serves as a reliable proxy for corrosion severity. We note that longer distances (e.g., 11 cm) may introduce slight contour distortion due to reduced imaging resolution (Fig. 16). In such cases, by performing periodic controlled measurements, one can still leverage `MagLens` to assess the process of corrosion.

7.6 Efficacy of Physics-informed Synthesis

To evaluate the efficacy of our physics-informed synthetic dataset and real-data fine-tuning, we pretrain the model on synthesized data (Sec. 5.2) and assess transfer to real measurements by fine-tuning under five budgets (0, 180, 360, 540, and 720 samples), where

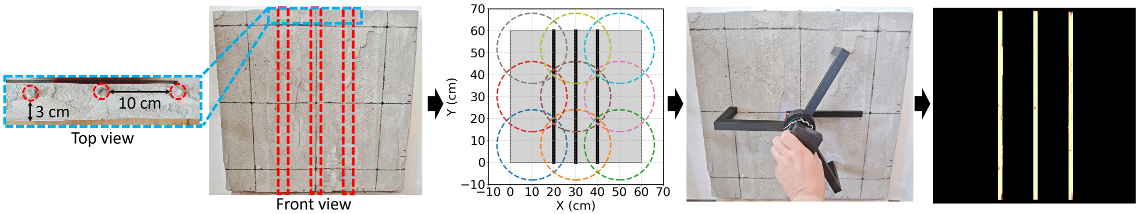

(a) Concrete wall testbed (b) Scan path planning (c) Handheld scanning (d) Stitched imaging results

Figure 26: End-to-end wall testbed scanning and reconstruction process.

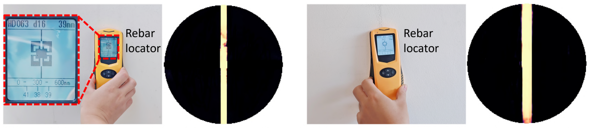

(a) Real wall with 16 mm rebar at 39 mm cover depth (b) Real wall with 20 mm rebar at 15 mm cover depth

Figure 27: Rebar locator vs. MagLens on two real walls.

0 denotes the baseline model without fine-tuning. We evaluate on the default rebar and repeat each configuration five times. As shown in Fig. 23, MagLens achieves average IoU scores of 0.82, 0.89, 0.94, 0.97, and 0.98 at 0, 180, 360, 540, and 720 samples, respectively. The average distance errors are 0.66 cm, 0.46 cm, 0.39 cm, 0.30 cm, and 0.29 cm. The baseline model achieves an IoU of 0.82, indicating that our physics-informed synthesis captures geometry-relevant patterns. Thus, MagLens is readily extensible to diverse ferrous objects via the automated synthesis pipeline (Sec. 5.2). Note that adding a limited amount of real data (e.g., 180 samples) improves performance by narrowing the simulation-to-real domain gap. As performance is nearly stable beyond 540 samples, 720 samples (i.e., 2.6% of the dataset) constitute a practical fine-tuning size.

7.7 Imaging Metal Studs and Iron Pipes

We evaluate MagLens on a C-shaped galvanized metal stud and two cast iron pipe elbows of different sizes and curvatures, representing typical ferrous components with diverse geometries and materials. As shown in Fig. 24, MagLens accurately reconstructs the contours of all three objects, achieving IoU scores of 0.95 for the metal stud and 0.96/0.94 for the two iron pipes, with distance errors below 0.30 cm. The consistent performance across these materials indicates that MagLens primarily leverages geometry-dependent magnetic patterns rather than material-specific signatures, as supported by the magnetization diversity in our synthetic dataset (Sec. 5.2).

7.8 Generalization to Unseen Geometries

To assess the practical generalization of MagLens, we evaluate MagLens on geometries not seen during the training phase. We test three ferrous objects with distinct geometries: a disc spring, a pipe-wrench hook jaw, and a pair of garden shears, using the default model configuration. As shown in Fig. 25, MagLens reconstructs their contours with IoU scores of 0.82, 0.85, and 0.82, respectively, and depth errors below 0.5 cm.

7.9 End-to-end Wall Inspection

We construct a 60 cm × 60 cm concrete wall testbed with three vertically aligned rebars (12 mm in diameter, 60 cm in length) embedded 10 cm apart at a 3 cm cover depth, reflecting a typical reinforcement layout (Fig. 26(a)). For realistic deployment, the wall is mounted vertically and MagLens is operated in a handheld configuration. Considering MagLens' effective sensing radius of 16 cm, complete wall coverage requires multiple sensing passes. To ensure full coverage with minimal overlap, we adopt a tiled scanning strategy that computes an optimized set of scan centers based on wall dimensions (Fig. 26(b)). These centers are marked on the wall surface to guide the user, and at each point MagLens performs a handheld 360° sweep to capture magnetic data (Fig. 26(c)). The resulting patches are then geometrically aligned and stitched into a global composite using their known spatial offsets. As shown in Fig. 26(d), the reconstruction recovers all three rebars and their spatial layout, achieving an IoU score of 0.94 with a distance error below 0.35 cm. This demonstrates that MagLens supports large-area inspection in real-world scenarios by integrating multiple local scans. The full inspection requires 12 minutes, including four minutes for marking and eight minutes for nine scans. This scanning time is comparable to commercial GPR systems, which require 10 minutes for a 2 ft × 2 ft (i.e., 61 cm × 61 cm) area [18]. Note that the scanning time can be further reduced by increasing the rotational speed (Sec. 7.3.7).

7.10 Robustness in Real-world Walls

7.10.1 Impact of power cables. Nearby non-ferrous components (e.g., copper/aluminum) do not retain remanence [55] and thus have limited impact on MagLens' imaging. Walls may also embed time-varying electromagnetic interference (EMI) sources [68, 90], such as AC power cables. To assess their impact, we locate an in-wall power cable with a commercial AC detector and then perform a rotational scan with MagLens directly above the identified position. The measured magnetic field variation of all three axes remains below 1 μT, negligible compared to the rebar-induced signatures (i.e., > 10 μT in Fig. 7). This robustness arises from two factors: (i) indoor 50/60 Hz magnetic fields (ELF) are generally weak — around 0.11 μT according to WHO [93]; and (ii) the RM3100's sampling configuration (i.e., 60 Hz) effectively mitigates AC magnetic fields.

7.10.2 Real-world wall inspection. To further validate MagLens' usability, we scan two real building walls with different rebar diameters and cover depths. Since destructive verification (e.g., drilling) is infeasible due to structural integrity concerns, we use a rebar locator's estimation as the reference for comparison. As shown in Fig. 27, one site includes a 16 mm rebar at 39 mm depth, and the other a 20 mm rebar at 15 mm depth. At the same test positions as the locator, MagLens reconstructs the contours and estimates the diameters via pixel-to-metric scaling. The estimated diameters (14.8 mm and 22.6 mm) and depths (41.0 mm and 15.7 mm) align closely with the locator's readings. Compared to the locator, MagLens further provides detailed contour reconstruction.

7.11 Overhead of MagLens

The sensor array consumes < 0.5 W and supports 1.5 hours of operation with a 200 mAh Li-Po battery. This duration allows coverage of a 3 m × 1 m wall segment under our default scanning configuration. The rotational scanning unit consumes 6.24 W and operates for five hours on a 12 V, 2,000 mAh battery. For computational efficiency, we benchmark the inference pipeline on an RTX 3090 GPU. Each prediction requires about 275 ms, enabling real-time imaging.

8 Related Works

8.1 Magnetic Field Visualization

Magnetic field visualization captures the spatial distribution of flux for sensing and diagnostic purposes. [48] proposes a system combining Helmholtz coils with a 20 × 20 sensor array to visualize magnetic responses for nuclear safety inspection. Although effective in controlled settings, the system's bulky setup and extremely close sensing range (1–2 mm) render it infeasible for structural inspection tasks. The magnetic field camera [84] employs a 2D array for visualization of nearby magnetic fields. To enhance spatial resolution, [39] constructs a dense Hall element array system. However, such systems demand precise calibration, intricate circuitry, and static deployment, limiting their scalability. Low-cost magnetic viewing films [4] provide intuitive visual feedback based on local field strength. Despite their simplicity, these films operate only at contact range and require strong magnetic signals.

8.2 Ferrous Structure Inspection

Various techniques have been proposed to inspect embedded ferrous structures. Electrochemical methods including half-cell potential [41, 53, 64] and linear polarization resistance [37, 61, 66, 74] are widely used to estimate corrosion risk by measuring electrical properties through direct contact with exposed components. While effective for degradation assessment, these methods are invasive and cannot localize damage within intact structures. Ultrasonic methods [36, 52, 69] detect delamination or cracks through pulse velocity analysis. GPR-based systems [38, 57, 70] emit electromagnetic pulses and analyze reflections to detect subsurface features. IR-UWB systems such as SiWa [95] leverage deep UWB radar and neural networks to detect embedded objects, but are still limited by RF resolution and cannot recover object contours or precise geometry. Emerging magnetism-based systems, such as iCAMM [21] and IGS [28], utilize high-sensitivity magnetometers to detect magnetic anomalies for assessing potential corrosion or deterioration of rebars. However, they lack localization capability, fine-grained contour recovery, and applicability to other ferrous structures.

9 Discussion

9.1 Applications

Fracture detection. Fractures are severe anomalies caused by material deterioration or fatigue, yet their subtle signatures make non-invasive detection highly challenging. We conducted a preliminary experiment by scanning an iron plate with an emulated fracture, implemented as a 0.1 mm gap (the thickness of an A4 paper) between two segments (Fig. 28(a)). As shown in Fig. 28(b), the z-axis field map reveals distinct perturbations at the fracture location. By incorporating such patterns into the synthetic training dataset, MagLens could detect cracks in ferrous materials (Fig. 28(c)).

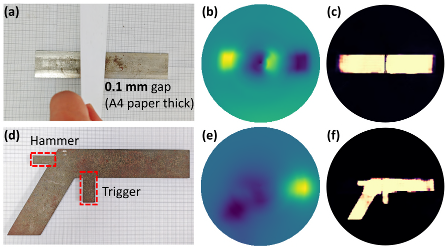

Figure 28: MagLens' applicability to structural fracture detection (a—c) and safety inspection (d–f).

Safety inspection. Conventional safety screening methods suffer key limitations. Millimeter-wave systems cannot penetrate water or thick clothing [3] and X-rays raise health concerns. In contrast, magnetic fields penetrate water [88] and present no safety risks. To explore this potential, we fabricated a handgun-shaped iron plate incorporating features such as the trigger and hammer (Fig. 28(d)) and scanned it with MagLens. The z-axis field map reveals distinctive patterns consistent with the object's geometry (Fig. 28(e)). By augmenting the synthetic dataset with diverse weapon profiles, MagLens reconstructs the contour and structural details (Fig. 28(f)).

9.2 Improving MagLens

Multi-object imaging. Real walls contain multiple ferrous objects, whose remanent fields may overlap and produce ambiguous spatial patterns. To cover such cases, our synthesized training set already includes 21.4% multi-object scenes (Table. 1), spanning representative multi-rebar layouts. This coverage aligns with our end-to-end wall inspection results (Sec. 7.9). Walls may also contain mixed ferrous elements (e.g., rebars with pipes/studs), which can introduce more complex magnetic patterns. Our modular synthesis pipeline can incorporate additional object types to generate mixed-type multi-object scenes, improving robustness in such in-wall layouts.

Uneven wall surfaces. In real deployments, uneven wall surfaces can introduce air gaps and varying standoff during scanning. MagLens mitigates this effect by explicitly estimating cover depth and applying distance-aware scaling. To further cover uneven-contact conditions, our synthetic pipeline can model tilted targets and non-uniform stand-off variations. The spacer blocks (Fig. 6(b)) also help maintain stable contact geometry on uneven surfaces.

10 Conclusion

We have presented MagLens, the first low-cost and mobile imaging platform capable of reconstructing the contours of everyday ferrous objects such as rebars, metal studs and iron pipes. Unlike traditional inspection tools, MagLens combines synthetic-aperture magnetic sensing with a physics-informed neural imaging pipeline to transform weak remanent fields into fine-grained geometric reconstruction. MagLens has immediate applicability for inspecting the condition of safety-critical ferrous infrastructure and systems. With these unique advantages, we believe MagLens opens the door to practical imaging for large-scale inspection of critical structures.

Acknowledgments

We thank the anonymous reviewers and shepherd for their suggestions. This work was supported by the National Natural Science Foundation of China under Grant No. 62472283. Dongyao Chen is the corresponding author.

References

[1] 2003. SPI Protocol. https://web.archive.org/web/20150413003534/http://www.ee.nmt.edu/~teare/ee308l/datasheets/S12SPIV3.pdf.

[2] 2008. *Domains and the Magnetization Process*. John Wiley & Sons, Ltd, Chapter 9, 275–333. doi:10.1002/9780470386323.ch9 arXiv:https://onlinelibrary.wiley.com/doi/pdf/10.1002/9780470386323.ch9

[3] 2011. Sweating Bullets: Body Scanners Can See Perspiration as a Potential Weapon. https://www.propublica.org/article/sweating-bullets-body-scanners-can-see-perspiration-as-a-potential-weapon.

[4] 2013. Green Magnetic Field Viewing Film. https://cmsmagnetics.com/neo.php

[5] 2017. GSSI Handbook For Concrete Inspection. https://www.geophysical.com/wp-content/uploads/2017/10/GSSI-Concrete-Handbook.pdf.

[6] 2018. RAYTAC MDBT42Q-512KV2. https://www.raytac.com/product/ins.php?index_id=31.

[7] 2018. RM3100 Magneto-Inductive Magnetometer. https://www.pnisensor.com/rm3100/.

[8] 2019. Details and Detailing of Concrete Reinforcement. https://regbar.com/wp-content/uploads/2019/09/ACI-315.pdf.

[9] 2020. ASTM C754-20: Standard Specification for Installation of Steel Framing Members to Receive Screw-Attached Gypsum Panel Products. https://www.astm.org/c0754-20.html

[10] 2022. ACI CODE-318-19(22): Building Code Requirements for Structural Concrete and Commentary (Reapproved 2022). https://www.concrete.org/store/productdetail.aspx?ItemID=318U19&Language=English&Units=US_Units

[11] 2022. Building Safety Act 2022. https://www.legislation.gov.uk/ukpga/2022/30/contents.

[12] 2022. Florida Legislature Passes Bill Requiring Stricter Inspections for Condominiums. https://www.iccsafe.org/about/periodicals-and-newsroom/florida-legislature-passes-bill-requiring-stricter-inspections-for-condominiums/.

[13] 2024. Melexis: MLX90393 Triaxis Micropower Magnetometer. https://www.melexis.com/-/media/files/documents/datasheets/mlx90393-datasheet-melexis.pdf.

[14] 2024. Surfside condo collapse investigators provide key insights into possible causes of the disaster. Here are the top takeaways. https://edition.cnn.com/2024/03/08/us/surfside-condo-collapse-investigation-takeaways.

[15] 2025. A1040 MIRA 3D ultrasonic tomography. https://www.novatest.it/en/civil-engineerings/a1040-mira-3d/.

[16] 2025. Eurocode 2: Design of concrete structures. https://eurocodes.jrc.ec.europa.eu/EN-Eurocodes/eurocode-2-design-concrete-structures.

[17] 2025. Green Magnetic Flux Viewing Film for Revealing Hidden Magnetic Field Patterns. https://www.amazon.ae/CMS-MAGNETICS-Revealing-Permanent-Education/dp/B0B5YJ8CWM.

[18] 2025. Ground Penetrating Radar (GPR). https://www.aelinspector.com/ground-penetrating-radar.

[19] 2025. HallinSight 3D-Hall Magnetic Field Camera. https://www.magnergytech.com/product/hallinsight-3d-hall-magnetic-field-camera/.

[20] 2025. Hot spot detection—what to look for. https://www.fluke.com/en/learn/blog/thermal-imaging/hot-spot-detection.

[21] 2025. iCAMM Inspection Platform. https://www.inspecterra.com/en/services.

[22] 2025. Langry LR-G200 Integrated Rebar Scanner. https://www.langryndt.com/rebar-scanners-a-comprehensive-comparison/.

[23] 2025. Magnetic Domains. https://nationalmaglab.org/magnet-academy/watch-play/interactive-tutorials/magnetic-domains/.

[24] 2025. makita HR4003C Rotary Hammer Instruction Manual. https://manuals.plus/makita/hr4003c-rotary-hammer-manual.

[25] 2025. Metrolab HallinSight 3-D-Hall Magnetic Field Camera. https://gmw.com/product/hallinsight-3-d-hall-magnetic-field-camera/.

[26] 2025. New York City's Facade Inspection & Safety Program (FISP). https://www.locallaw11.com/.

[27] 2025. Proceq Ground Penetrating Radars GP8000. https://www.screeningeagle.com/en/products/proceq-gp8000.

[28] 2025. Rebar deterioration inspection system. https://www.igs-group.com/en/solutions/infrastructure.

[29] 2025. Reinforced concrete. https://en.wikipedia.org/wiki/Reinforced_concrete.

[30] 2025. STM32F103C8T6 micro controller. https://www.st.com/en/microcontrollers-microprocessors/stm32f103c8.html.

[31] Mohamed A. Abdelhafez, Bruce Ellingwood, and Hussam Mahmoud. 2022. Hidden costs to building foundations due to sea level rise in a changing climate. *Scientific Reports* 12, 1 (2022), 14020. doi:10.1038/s41598-022-18467-3

[32] Nabila Abraham and Naimul Mefraz Khan. 2019. A Novel Focal Tversky Loss Function With Improved Attention U-Net for Lesion Segmentation. In *2019 IEEE 16th International Symposium on Biomedical Imaging (ISBI 2019)*. 683–687. doi:10.1109/ISBI.2019.8759329

[33] Alaa Agala, Muhammad Khan, and Andrew Starr. 2023. Degradation mechanisms associated with metal pipes and the effective impact of LDMs and LLMs in water transport and distribution. *Proceedings of the Institution of Mechanical Engineers, Part C: Journal of Mechanical Engineering Science* 237, 8 (2023), 1855–1876. doi:10.1177/09544062221133948 arXiv:https://doi.org/10.1177/09544062221133948

[34] Carmen Andrade and C Alonso. 2004. Test methods for on-site corrosion rate measurement of steel reinforcement in concrete by means of the polarization resistance method. *Materials and structures* 37, 9 (2004), 623–643.

[35] Michael Angermann, Martin Frassl, Marek Doniec, Brian J. Julian, and Patrick Robertson. 2012. Characterization of the indoor magnetic field for applications in Localization and Mapping. In *2012 International Conference on Indoor Positioning and Indoor Navigation (IPIN)*. 1–9. doi:10.1109/IPIN.2012.6418864

[36] C. Aristégui, M.J.S. Lowe, and P. Cawley. 2001. Guided waves in fluid-filled pipes surrounded by different fluids. *Ultrasonics* 39, 5 (2001), 367–375. doi:10.1016/S0041-624X(01)00064-6

[37] Pejman Azarsa and Rishi Gupta. 2017. Electrical resistivity of concrete for durability evaluation: a review. *Advances in Materials Science and Engineering* 2017, 1 (2017), 8453095.

[38] Paola Boldrin, Giacomo Fornasari, and Enzo Rizzo. 2024. Review of Ground Penetrating Radar Applications for Bridge Infrastructures. *NDT* 2, 1 (2024), 53–75. doi:10.3390/ndt2010004

[39] Jiangwei Cai, Tan Zhou, Yishen Xu, and Xin Zhu. 2024. A High-Resolution Magnetic Field Imaging System Based on the Unpackaged Hall Element Array. *Applied Sciences* 14, 13 (2024). doi:10.3390/app14135788

[40] Hu Cao, Yueyue Wang, Joy Chen, Dongsheng Jiang, Xiaopeng Zhang, Qi Tian, and Manning Wang. 2023. Swin-Unet: Unet-Like Pure Transformer for Medical Image Segmentation. In *Computer Vision – ECCV 2022 Workshops*, Leonid Karlinsky, Tomer Michaeli, and Ko Nishino (Eds.). Springer Nature Switzerland, Cham, 205–218.

[41] Parham Chabi, O Burkan Isgor, Beatriz Martin-Perez, and Pouria Ghods. 2013. Effectiveness of half-cell potential mapping in corrosion assessment of reinforcement in loaded concrete bridge decks. In *3rd Specialty Conference on Material Engineering & Applied Mechanics. Montreal, Quebec*. 1–9.

[42] Dongyao Chen, Mingke Wang, Chenxi He, Qing Luo, Yasha Iravantchi, Alanson Sample, Kang G. Shin, and Xinbing Wang. 2021. MagX: wearable, untethered hands tracking with passive magnets. In *Proceedings of the 27th Annual International Conference on Mobile Computing and Networking* (New Orleans, Louisiana) *(MobiCom '21)*. Association for Computing Machinery, New York, NY, USA, 269–282. doi:10.1145/3447993.3483260

[43] Ting Chen, Simon Kornblith, Mohammad Norouzi, and Geoffrey Hinton. 2020. A simple framework for contrastive learning of visual representations. In *Proceedings of the 37th International Conference on Machine Learning (ICML'20)*. JMLR.org, Article 149, 11 pages.

[44] Zhenyu Chen, Peihang Chen, Jingyuan Huang, and Dongyao Chen. 2025. Towards Extended Interaction with Differential Magnetic Tracking and Deep Learning. *International Journal of Human–Computer Interaction* 0, 0 (2025), 1–24. doi:10.1080/10447318.2025.2565394 arXiv:https://doi.org/10.1080/10447318.2025.2565394

[45] Zhenyu Chen, Jike Wang, and Dongyao Chen. 2024. Demo: Implementation and Benchmark of Magnetic Tracking on Mobile Platforms. In *Proceedings of the 2024 Workshop on Adaptive AIoT Systems* (Minato-ku, Tokyo, Japan) *(AdaAIoTSys '24)*. Association for Computing Machinery, New York, NY, USA, 21–22. doi:10.1145/3662007.3663885

[46] S. Chikazumi. 2009. *Physics of Ferromagnetism*. OUP Oxford. https://books.google.com/books?id=AZVfuxXF2GsC

[47] I.S. Cole and D. Marney. 2012. The science of pipe corrosion: A review of the literature on the corrosion of ferrous metals in soils. *Corrosion Science* 56 (2012), 5–16. doi:10.1016/j.corsci.2011.12.001

[48] Brendan J. Darrer, Joe C. Watson, Paul Bartlett, and Ferruccio Renzoni. 2015. Magnetic Imaging: a New Tool for UK National Nuclear Security. *Scientific Reports* 5, 1 (22 Jan 2015), 7944. doi:10.1038/srep07944

[49] Rong Ding, Haiming Jin, Dong Xiang, Xiaocheng Wang, Yongkui Zhang, Dingman Shen, Lu Su, Wentian Hao, Mingyuan Tao, Xinbing Wang, and Chenghu Zhou. 2023. Soil Moisture Sensing with UAV-Mounted IR-UWB Radar and Deep Learning. *Proc. ACM Interact. Mob. Wearable Ubiquitous Technol.* 7, 1, Article 11 (March 2023), 25 pages. doi:10.1145/3580867

[50] Laura Dodds, Tara Boroushaki, Kaichen Zhou, and Fadel Adib. 2025. Non-Line-of-Sight 3D Object Reconstruction via mmWave Surface Normal Estimation. In *Proceedings of the 23rd Annual International Conference on Mobile Systems, Applications and Services* (Anaheim, CA, USA) *(MOBISYS '25)*. Association for Computing Machinery, New York, NY, USA, 14 pages. doi:10.1145/3711875.3729138

[51] Laura Dodds, Hailan Shanbhag, Junfeng Guan, Saurabh Gupta, and Haitham Hassanieh. 2024. Around the Corner mmWave Imaging in Practical Environments. In *Proceedings of the 30th Annual International Conference on Mobile Computing and Networking* (Washington D.C., DC, USA) *(ACM MobiCom '24)*. Association for Computing Machinery, New York, NY, USA, 953–967. doi:10.1145/3636534.3690671

[52] Mahjoub El Mountassir, Slah Yaacoubi, and Fethi Dahmene. 2020. Reducing false alarms in guided waves structural health monitoring of pipelines: Review synthesis and debate. *International Journal of Pressure Vessels and Piping* 188 (2020), 104210. doi:10.1016/j.ijpvp.2020.104210

[53] Bernhard Elsener, C Andrade, Joost Gulikers, Rob Polder, and Michael Raupach. 2003. Half-cell potential measurements—Potential mapping on reinforced concrete structures. *Materials and Structures* 36, 7 (2003), 461–471.

[54] Paweł Karol Frankowski and Tomasz Chady. 2023. A Comparative Analysis of the Magnetization Methods Used in the Magnetic Nondestructive Testing of Reinforced Concrete Structures. *Materials* 16, 21 (2023). doi:10.3390/ma16217020

[55] Michele Gaeta, Marco Cavallaro, Sergio Lucio Vinci, Enricomaria Mormina, Alfredo Blandino, Maria Adele Marino, Francesca Granata, Agostino Tessitore, Karol Galletta, Tommaso D'Angelo, et al. 2021. Magnetism of materials: theory and practice in magnetic resonance imaging. *Insights into Imaging* 12, 1 (2021), 179.

[56] Xiao gang Wang, Wei ping Zhang, Xiang lin Gu, and Hong chao Dai. 2013. Determination of residual cross-sectional areas of corroded bars in reinforced concrete structures using easy-to-measure variables. *Construction and Building Materials* 38 (2013), 846–853. doi:10.1016/j.conbuildmat.2012.09.060 25th Anniversary Session for ACI 228 – Building on the Past for the Future of NDT of Concrete.

[57] Iván Garrido, Mercedes Solla, Susana Lagüela, and Mezgeen Rasol. 2022. Review of InfraRed Thermography and Ground-Penetrating Radar Applications for Building Assessment. *Advances in Civil Engineering* 2022, 1 (2022), 5229911. doi:10.1155/2022/5229911 arXiv:https://onlinelibrary.wiley.com/doi/pdf/10.1155/2022/5229911

[58] Xiaofeng Han, Penggang Wang, Dongbo Cui, Taher A. Tawfik, Zhaoyi Chen, Li Tian, and Yizhi Gao. 2023. Rebar corrosion detection in concrete based on capacitance principle. *Measurement* 209 (2023), 112526. doi:10.1016/j.measurement.2023.112526

[59] Xian-Feng Han, Hamid Laga, and Mohammed Bennamoun. 2021. Image-Based 3D Object Reconstruction: State-of-the-Art and Trends in the Deep Learning Era. *IEEE Transactions on Pattern Analysis and Machine Intelligence* 43, 5 (2021), 1578–1604. doi:10.1109/TPAMI.2019.2954885

[60] Roger F. Harrington. 1993. *Field Computation by Moment Methods.* Wiley-IEEE Press.

[61] Karla Hornbostel, Claus K Larsen, and Mette R Geiker. 2013. Relationship between concrete resistivity and corrosion rate–A literature review. *Cement and concrete composites* 39 (2013), 60–72.

[62] Nozhan Hosseini, Mahfuza Khatun, Changyu Guo, Kairui Du, Ozgur Ozdemir, David W. Matolak, Ismail Guvenc, and Hani Mehrpouyan. 2021. Attenuation of Several Common Building Materials: Millimeter-Wave Frequency Bands 28, 73, and 91 GHz. *IEEE Antennas and Propagation Magazine* 63, 6 (2021), 40–50. doi:10.1109/MAP.2020.3043445

[63] David Jiles. 2015. *Introduction to Magnetism and Magnetic Materials* (3rd ed.). CRC Press.

[64] Charles Kennedy. 2021. Reinforcing Steel Corrosion Potential Probability Evaluation using Electrochemical Hall-Cell Measurement. *GSJ* 9, 7 (2021).

[65] Ayca Kirimtat and Ondrej Krejcar. 2018. A review of infrared thermography for the investigation of building envelopes: Advances and prospects. *Energy and Buildings* 176 (2018), 390–406. doi:10.1016/j.enbuild.2018.07.052

[66] Hamed Layssi, Pouria Ghods, Aali R Alizadeh, and Mustafa Salehi. 2015. Electrical resistivity of concrete. *Concrete international* 37, 5 (2015), 41–46.

[67] Chen-Wei Liang, Ertan Balaban, Ehsan Ahmad, Zhichao Zhang, James Sexton, and Mohamed Missous. 2017. A real time high sensitivity high spatial resolution quantum well hall effect magnetovision camera. *Sensors and Actuators A: Physical* 265 (2017), 127–137. doi:10.1016/j.sna.2017.08.035

[68] Chris Xiaoxuan Lu, Yang Li, Peijun Zhao, Changhao Chen, Linhai Xie, Hongkai Wen, Rui Tan, and Niki Trigoni. 2018. Simultaneous Localization and Mapping with Power Network Electromagnetic Field. In *Proceedings of the 24th Annual International Conference on Mobile Computing and Networking* (New Delhi, India) *(MobiCom '18)*. Association for Computing Machinery, New York, NY, USA, 607–622. doi:10.1145/3241539.3241540

[69] Feng Lyu, Xinyue Zhou, Zheng Ding, Xinglong Qiao, and Dan Song. 2024. Application Research of Ultrasonic-Guided Wave Technology in Pipeline Corrosion Defect Detection: A Review. *Coatings* 14, 3 (2024). doi:10.3390/coatings14030358

[70] Yuri Álvarez López, María García-Fernández, Guillermo Álvarez Narciandi, and Fernando Las-Heras Andrés. 2022. Unmanned Aerial Vehicle-Based Ground-Penetrating Radar Systems: A review. *IEEE Geoscience and Remote Sensing Magazine* 10, 2 (2022), 66–86. doi:10.1109/MGRS.2022.3160664

[71] Markus Marks, Manuel Knott, Neehar Kondapaneni, Elijah Cole, Thijs Defraeye, Fernando Perez-Cruz, and Pietro Perona. 2025. A closer look at benchmarking self-supervised pre-training with image classification. *International Journal of Computer Vision* (2025), 1–13.

[72] Fausto Milletari, Nassir Navab, and Seyed-Ahmad Ahmadi. 2016. V-Net: Fully Convolutional Neural Networks for Volumetric Medical Image Segmentation. In *2016 Fourth International Conference on 3D Vision (3DV)*. 565–571. doi:10.1109/3DV.2016.79

[73] Alberto Moreira, Pau Prats-Iraola, Marwan Younis, Gerhard Krieger, Irena Hajnsek, and Konstantinos P. Papathanassiou. 2013. A tutorial on synthetic aperture radar. *IEEE Geoscience and Remote Sensing Magazine* 1, 1 (2013), 6–43. doi:10.1109/MGRS.2013.2248301

[74] W Morris, A Vico, M Vazquez, and SR De Sanchez. 2002. Corrosion of reinforcing steel evaluated by means of concrete resistivity measurements. *Corrosion Science* 44, 1 (2002), 81–99.

[75] M. Mosharafi, S.B. Mahbaz, and M.B. Dusseault. 2020. Bridge deck assessment using infrastructure corrosion assessment magnetic method (iCAMM™) technology, a case study of a culvert in Markham city, Ontario, Canada. *NDT & E International* 116 (2020), 102356. doi:10.1016/j.ndteint.2020.102356

[76] Erato Ch. Oikonomopoulou, Vasiliki A. Palieraki, Ioannis P. Sfikas, and Constantinos G. Trezos. 2022. Reliability and limitations of GPR for identifying objects embedded in concrete – Experience from the lab. *Case Studies in Construction Materials* 16 (2022), e00898. doi:10.1016/j.cscm.2022.e00898

[77] ASTM Committee G-1 on Corrosion of Metals et al. 2017. *Standard practice for preparing, cleaning, and evaluating corrosion test specimens.* ASTM international.

[78] Michael Ortner and Lucas Gabriel Coliado Bandeira. 2020. Magpylib: A free Python package for magnetic field computation. *SoftwareX* 11 (2020), 100466.

[79] Harsh Rathod, Scott Debeck, Rishi Gupta, and Brian Chow. 2019. Applicability of GPR and a rebar detector to obtain rebar information of existing concrete structures. *Case Studies in Construction Materials* 11 (2019), e00240. doi:10.1016/j.cscm.2019.e00240

[80] Romain Rodrigues, Stéphane Gaboreau, Julien Gance, Ioannis Ignatiadis, and Stéphanie Betelu. 2021. Reinforced concrete structures: A review of corrosion mechanisms and advances in electrical methods for corrosion monitoring. *Construction and Building Materials* 269 (2021), 121240. doi:10.1016/j.conbuildmat.2020.121240

[81] Behrouz Shafei, Weizhuo Shi, et al. 2022. *Steel Reinforcement Section Loss Guidance Tables.* Technical Report. Minnesota. Department of Transportation. Office of Research & Innovation.

[82] Ruiyi Shen and Yasaman Ghasempour. 2023. Scattering from Rough Surfaces in 100+ GHz Wireless Mobile Networks: From Theory to Experiments. In *Proceedings of the 29th Annual International Conference on Mobile Computing and Networking* (Madrid, Spain) *(ACM MobiCom '23)*. Association for Computing Machinery, New York, NY, USA, Article 92, 15 pages. doi:10.1145/3570361.3613306

[83] Vaclav Smil. 2016. *Still the iron age: iron and steel in the modern world.* Butterworth-Heinemann.

[84] Andriyan Bayu Suksmono, Donny Danudirdjo, Antonius Darma Setiawan, Dien Rahmawati, and Rizki Putra Prastio. 2021. A Magnetic Field Camera for Real-Time Subsurface Imaging Applications. *Applied Sciences* 11, 8 (2021). doi:10.3390/app11083302

[85] Philippe Thévenaz, Thierry Blu, and Michael Unser. 2000. 25 - Image Interpolation and Resampling. In *Handbook of Medical Imaging*, ISAAC N. BANKMAN (Ed.). Academic Press, San Diego, 393–420. doi:10.1016/B978-012077790-7/50030-8

[86] Ko Tomita and Michael Yit Lin Chew. 2022. A Review of Infrared Thermography for Delamination Detection on Infrastructures and Buildings. *Sensors* 22, 2 (2022). doi:10.3390/s22020423

[87] Jike Wang, Yasha Iravantchi, Alanson Sample, Kang G. Shin, Xinbing Wang, and Dongyao Chen. 2024. Polaris: Accurate, Vision-free Fiducials for Mobile Robots with Magnetic Constellation. In *Proceedings of the 30th Annual International Conference on Mobile Computing and Networking* (Washington D.C., DC, USA) *(ACM MobiCom '24)*. Association for Computing Machinery, New York, NY, USA, 1560–1574. doi:10.1145/3636534.3690711

[88] Jike Wang, Shanmu Wang, Yasha Iravantchi, Mingke Wang, Alanson Sample, Kang G. Shin, Xinbing Wang, Chenghu Zhou, and Dongyao Chen. 2024. METRO: Magnetic Road Markings for All-weather, Smart Roads. In *Proceedings of the 21st ACM Conference on Embedded Networked Sensor Systems* (, Istanbul, Turkiye,) *(SenSys '23)*. Association for Computing Machinery, New York, NY, USA, 280–293. doi:10.1145/3625687.3625809

[89] Mingke Wang, Qing Luo, Yasha Iravantchi, Xiaomeng Chen, Alanson Sample, Kang G. Shin, Xiaohua Tian, Xinbing Wang, and Dongyao Chen. 2022. Automatic calibration of magnetic tracking. In *Proceedings of the 28th Annual International Conference on Mobile Computing And Networking* (Sydney, NSW, Australia) *(MobiCom '22)*. Association for Computing Machinery, New York, NY, USA, 391–404. doi:10.1145/3495243.3558760

[90] Rongrong Wang, Rui Tan, Zhenyu Yan, and Chris Xiaoxuan Lu. 2024. Orientation-Aware 3D SLAM in Alternating Magnetic Field from Powerlines. *Proc. ACM Interact. Mob. Wearable Ubiquitous Technol.* 7, 4, Article 182 (Jan. 2024), 25 pages. doi:10.1145/3631446

[91] Yida Wang, Yu Lu, Yuxuan ZHOU, Yifei Shen, Lili Qiu, Zeyuan Lai, Yi-Chao Chen, Hao Pan, Juntao Zhou, Dian Ding, Mei Wang, Guangtao Xue, and Qian Zhang. 2025. High-resolution mmWave Imaging using Metasurface and Diffusion. In *Proceedings of the 23rd Annual International Conference on Mobile Systems, Applications and Services* (Anaheim, CA, USA) *(MOBISYS '25)*. Association for Computing Machinery, New York, NY, USA, 14 pages. doi:10.1145/3711875.3729162

[92] Zhongkun Wang, Jing Yu, Gengying Li, Min Zhang, and Christopher K.Y. Leung. 2019. Corrosion behavior of steel rebar embedded in hybrid CNTs-OH/polyvinyl alcohol modified concrete under accelerated chloride attack. *Cement and Concrete Composites* 100 (2019), 120–129. doi:10.1016/j.cemconcomp.2019.02.013

[93] World Health Organization. 2007. *Extremely Low Frequency Fields: Environmental Health Criteria 238.* World Health Organization, Geneva, Switzerland.

[94] Kai Yao, Kai Shen, Zheng-Dao Wang, and Yue-Sheng Wang. 2014. Three-dimensional finite element analysis of residual magnetic field for ferromagnets under early damage. *Journal of Magnetism and Magnetic Materials* 354 (2014), 112–118. doi:10.1016/j.jmmm.2013.10.047

[95] Tianyue Zheng, Zhe Chen, Jun Luo, Lin Ke, Chaoyang Zhao, and Yaowen Yang. 2021. SiWa: see into walls via deep UWB radar. In *Proceedings of the 27th Annual International Conference on Mobile Computing and Networking* (New Orleans, Louisiana) *(MobiCom '21)*. Association for Computing Machinery, New York, NY, USA, 323–336. doi:10.1145/3447993.3483258